



Dual-path Fe migration in the bulk phase reconstructing high quality Ni-O-Fe units for high efficient oxygen evolution reaction

Xiaobing Wang^{a,*}, Chengyu Wei^{b,1}, Xiaosheng Song^a, Zuohui Wang^{a,c,**}, Yong Zhao^{a,*}

^a Key Lab for Special Functional Materials of Ministry of Education, National & Local Joint Engineering Research Center for High-efficiency Display and Lighting Technology, Collaborative Innovation Center of Nano Functional Materials and Applications, College of Materials, Henan University, Kaifeng 475004, PR China

^b State Key Laboratory of Chem/Bio-Sensing and Chemometrics, Advanced Catalytic Engineering Research Center of the Ministry of Education, College of Chemistry and Chemical Engineering, Hunan University, Changsha 410082, PR China

^c Luoyang Inst Sci & Technol, Sch Elect Engrg & Automat, Luoyang, Henan 471023, PR China

ARTICLE INFO

Keywords:

Oxygen evolution reaction
Surface reconstruction
Element migration
Ni-O-Fe units
Electron transfer

ABSTRACT

In the oxygen evolution reaction (OER), the non-reversible destruction of surface electronic structure caused by the irregular element migration in complex surface/interface reaction limits the improvement of catalyst's activity and stability. Herein, we successfully realize the control of 'dual-path migration of metallic elements in OER' to stepwise reconstruct the O-coordinated bi-metal heterodimer (M_1 -O- M_2) for electron density redistribution. By designing $Fe@FeNi_3 @NiO-Fe_3O_4$ (F-FN-NFO) model electrode with stepwise surface treatment in OER process, the directional migration (from core to shell, *path 1*) and adjacent-surface migration of Fe atoms (*path 2*) are both controlled to reduce the formation energy of Ni-O-Fe units, realizing strengthened electron transfer between heterogeneous metal centers. After the surface reconstruction, the OER activity of F-FN-NFO increases for 8.6 times at 1.7 V (30.5–263 mA cm⁻²). Based on this strategy, the designed three-dimension $NiFe@NiFe_xO$ is positive activated compared to traditional $NiFe$ -oxidation with the overpotential reduced to 299 mV at 10 mA cm⁻².

1. Introduction

The oxygen evolution reaction (OER) of four-electron transport pathway is an indispensable reaction in photo-/electrocatalytic water electrolyzers [1–3] and metal-air aqueous batteries [4], but its low kinetic becomes the bottleneck for improving the energy transfer efficiency of above-mentioned devices [5]. Developing polymetallic catalysts with high electronegative difference between metal centers has attracted widespread attention, ascribing to its redistribution of surface electron density for reducing the OER overpotential [6,7]. However, the predesigned active units are always destruct under electro-oxidation conditions, resulting in the poor electronic transfer between metal centers that limits the improvement of OER performance [8]. Although many strategies have been applied to dynamic optimize the OER reconstruction process, such as the construction of metal dissolution-replenishment balance and the restriction of surface structure evolution [9–12], the destructed active units is hard to be repaired

during oxygen evolution due to the complex surface/interface reaction.

In dual/ternary transition metal based catalysts, O-coordinated bi-metal heterodimer (M_1 -O- M_2) acts as an electron transfer channel for bridging the metal centers, which is considered as core units for optimizing the surface electronic structure [13]. In M_1 -O- M_2 , the electron transfer and spin-flip hopping in π - π bond has a much higher efficiency for electron redistribution [14]. Zhongtao Li's research confirms that the charge transfer ratio in Co-O-V would increase for 5.3 times compared to common metal-oxygen binding (Co-O), and the charge offset is almost linear with OER activity [15]. Besides, Shannon S. Stahl's study finds that the electron transfer in the Ni-O-Fe unit not only helps strengthen Fe-O bond for the adsorption of oxygen intermediates, but also promotes the electrochemical inactive Ni^{2+} oxygenizing into high active $NiOOH$ sites to accelerate the O_2 evolution [16]. Considering the low content of M_1 -O- M_2 units in the active layer caused by serious surface phase separation, it is of great significance for the dynamic construction of M_1 -O- M_2 units in OER to realize the precise optimization

* Correspondence to: Key Lab for Special Functional Materials of Ministry of Education, College of Materials, Henan University, Kaifeng 475004, PR China.

** Corresponding author at: Luoyang Inst Sci & Technol, Sch Elect Engrg & Automat, Luoyang, Henan 471023, PR China.

E-mail addresses: 10330083@vip.henu.edu.cn (X. Wang), wzh0379@163.com (Z. Wang), zhaoyong@henu.edu.cn (Y. Zhao).

¹ Xiaobing Wang and Chengyu Wei contributed equally to this work.

of the surface electronic structure.

In recent years, a great deal of work on the formation mechanism of M_1 -O- M_2 units have been explored to realize its self-reconstruction during OER [17]. It is found that M_1 -O- M_2 unit prefers to form at the heterogeneous interface on the surface of catalyst. Based on this theory, Jiande Chen et al. modified FeO_x clusters on the surface of NiFe-LDH to in situ construct the $FeOOH$ //NiFe-LDH interface. The high oxidation of $FeOOH$ would strengthen the binding of $Fe^{(3+\delta)+}$ -O- Ni^{2+} unit, which significantly promotes the oxidation of Ni^{2+} for improving the OER reaction efficiency [17]. Wenxiu Yan et al. doped Fe^{3+} into $Ni(OH)_2$ nanosheets to construct the heterogeneous interface between FeO_x and metal Ni during OER, in which numerous Ni-O-Fe units would in situ form and promotes the molecular activation [18]. However, the high inherent atomic size mismatch in the heterogeneous interface leads to the high formation energy of M_1 -O- M_2 , which limits its content and makes it instable in OER process.

In this work, we proposed a new concept of 'dual-path migration strategy of metallic elements in OER' to stepwise reconstruct the M_1 -O- M_2 units, which dynamic optimizes the electronic structure for improving the OER kinetics. By designing $Fe@FeNi_3@NiO-Fe_3O_4$ model electrode with stepwise surface treatment (Plasma Ar/H_2O treating) in OER process, the directional migration (from core to shell, *path 1*) and adjacent-surface migration of Fe atoms (*path 2*) are both controlled to repair/construct Ni-O-Fe units. It is found that directional Fe migration can reduce the formation energy of Ni-O-Fe units by forming relaxed grain boundaries in $\gamma-Fe_2O_3$ ($1/8 V_{Fe}$)/NiOOH heterostructure (V_{Fe} represent Fe vacancy defect), while the adjacent-surface Fe migration would further stabilize the Ni-O-Fe electron transfer channel by replenishing the oxygen defects (V_O). Based on this design, the activity of F-FN-NFO electrode increases from 30.5 mA cm^{-2} to 263 mA cm^{-2} (8.6 times) at 1.7 V. Similarly, the treated three-dimension porous $NiFe@NiFe_xO$ electrode shows a low overpotential of 299 mV and stable working for more than 100 h at the current density of 10 mA cm^{-2} . This work provides a guidance for the development of advanced OER electrocatalysts and boosts the application potential for oxide materials in catalysis.

2. Experimental section

2.1. Chemicals

All chemicals are analytical grade reagents without further purification. Nickel sulfate ($NiSO_4 \cdot 6H_2O \geq 98.5\%$), iron sulfate ($FeSO_4 \cdot 7H_2O \geq 99\%$), zinc sulfate ($ZnSO_4 \cdot H_2O \geq 99\%$), sodium citrate ($C_6H_5Na_3O_7 \geq 90\%$), ammonium citrate ($C_6H_5O_7(NH_4)_3 \geq 98.5\%$), sodium hydroxide ($NaOH \geq 90\%$), potassium hydroxide ($KOH \geq 90\%$) and ethanol were purchased from Aladdin Reagent Co., Ltd, Shanghai, China. The titanium sheet (Ti) with a thickness of 0.15 mm was used as the substrate for electrodeposition.

The electroplating experimental was carried out in a two-electrode configuration with Ti sheet as the working electrode and nickel plate as the counter electrode placed in the electrochemical cell, the distance between the two electrodes is 2 cm. Before electrodeposition, both Ti sheet ($2 \text{ cm} \times 2 \text{ cm}$) and nickel plate were ultrasonically cleaned for 10 min with acetone, HCl, ethanol and deionized water, respectively. In this work, three kinds of solution are needed for electrodeposition:

Solution A: 100 mL electrolytes consists of $FeSO_4 \cdot 7H_2O$ (0.6 g), $C_6H_5O_7(NH_4)_3$ (2.25 g) and $C_6H_5Na_3O_7$ (11.69 g). The pH value of three solution was adjusted to ≈ 9 at 35°C with dilute NaOH solution.

Solution B: $NiSO_4 \cdot 6H_2O$ (5 g) is added in Solution A under the same conditions.

Solution C: $ZnSO_4 \cdot 6H_2O$ (5 g) is added in Solution B under the same conditions.

2.2. Preparation of $Fe@FeNi_3@NiO-Fe_3O_4$ and $FeNi_3@NiO-Fe_3O_4$ model electrode

Two step electrodeposition was proceed to synthesize $Fe@FeNi_3@NiO-Fe_3O_4$ sample. First, the Fe layer was obtained by electrodeposited in solution A for 120 s at the current density of 30 mA cm^{-2} . Second, the obtained sample was used as substrate for further electrodeposition 20 s in solution B. After washed by deionized water and dried on vacuum, $Fe@FeNi_3@NiO-Fe_3O_4$ was obtained with plasma (HarrickPDC-32 G-2) treating for 10 s (O_2), abbreviated as F-FN-NFO.

Under the same conditions, $FeNi_3@NiO-Fe_3O_4$ without Fe concentration gradient was produced by electrodeposition only in solution B for 60 s, abbreviated as FN-NFO.

2.3. Preparation of self-supporting $NiFe@NiFe_xO$ porous electrode with Fe concentration gradient

First, NiFe layer was prepared by electrodeposited for 4 h in solution C at the current density of 30 mA cm^{-2} . Then, the as-prepared sample was annealed at 550°C for 5 min (Ar atmosphere) with air cooling to room temperature, and adequately etched in KOH solution (3 M). After washing with deionized water and dried on vacuum, the film can be separated from the Ti sheet. Third, the obtained samples were dealt with plasma (O_2) treatment for 10 s and annealed at 400°C for 30 min with Ar flow. Then, a self-supporting $NiFe@NiFe_xO$ porous electrode that contains concentration gradient is prepared, named $NiFe@NiFe_xO-30 \text{ min}$.

According to the above preparation process, the $NiFe_xO$ sample was obtained without the annealing treatment at 400°C . Meanwhile, adjusting the annealing time to 10 min and 60 min, the $NiFe@NiFe_xO-10 \text{ min}$ and $NiFe@NiFe_xO-60 \text{ min}$ electrodes can be acquired.

2.4. Surface treatment on the prepared samples

First, the prepared sample is cycled to a stable state by CV test from 0.0 to 0.8 V versus $Ag/AgCl$ (saturated KCl) at a high scan rate of 50 mV s^{-1} . Then it is treated with plasma Ar/H_2O for 15 s as the first surface treatment. The plasma Ar/H_2O treated samples are labeled as *FN-NFO-p* and *F-FN-NFO-p*, respectively, in which different times of plasma treatment is marked by p1, p2 and p3. For further structure evaluation, the applied scan rate on CV cycling is changed to 10 mV s^{-1} .

2.5. Materials characterization

X-ray diffraction (XRD) patterns were measured using a D8-Advance/Bruker with $Cu K\alpha$ radiation ($k = 0.15405 \text{ nm}$). Scanning electron microscopy (SEM) was performed on a Nova Nano SEM 450 field emission scanning electron microscope operated at 10 kV with EDS detector. Transmission electron microscope (TEM) and high-resolution TEM (HRTEM) images were conducted on a JEM-2100 field-emission high-resolution transmission electron microscope operated at 200 kV. X-ray photoelectron spectra (XPS) were collected on an Escalab 250Xi X-ray photoelectron spectrometer (Thermo Fisher Scientific Inc.), using $Al K\alpha$ X-ray (300 W) as the excitation source. Simultaneously, Raman spectroscopy was conducted on Via Reflex instrument with an excitation laser of 532 nm.

2.6. Electrochemical characterizations

All electrochemical tests were conducted on CHI 760e electrochemical workstation, performed in a standard three-electrode electrochemical cell with O_2 -saturated KOH solution ($pH=14$) as electrolyte. A conventional three-electrode cell was used with the Platinum plate and $Ag/AgCl$ (saturated KCl solution) used as counter and reference electrodes, respectively. For OER test, all cyclic voltammetry (CV) curves were measured from 0.0 to 0.8 V versus $Ag/AgCl$ (saturated KCl) at a scan rate of 10 mV s^{-1} , the CV cycling is carried out at a scan rate of 50

mV s^{-1} . Chronopotentiometry measurement was performed at a current density of 10 mA cm^{-2} . The potential converted to reversible hydrogen electrode (RHE) using the next equation: $E_{\text{RHE}} = E_{\text{Ag/AgCl}} + 0.197 + 0.059 \times \text{pH}$.

3. Results and discussion

Under harsh alkaline OER conditions, most of the transition metal-based catalysts suffer from a serious surface reconstruction due to their thermodynamic instability, including metal ion dissolution and phase separation [17]. As shown in Scheme 1a, the uncontrolled surface reconstruction process of traditional NiFe-based catalysts would induce a dense active layer (NiOOH) that restricts the further activation of inner sites [19]. In this process, the electron structure such as Ni-O-Fe units would be destructed that inhibits the electronic connections between heterogeneous metals [17]. To reconstruct the Ni-O-Fe units, extra Fe atoms should be first introduced into active layer and bonded with NiOOH species. Scheme 1b presents a designed ‘dual-path Fe migration’ strategy by using a F-FN-NFO electrode (nano-scale thin shell) as a model. On the one hand, Fe atoms would partly migrate from the core part to the surface active layer in OER, which has been proved by our previous research [20]. On the other hand, the adjacent-surface Fe sites can be activated if the dense reconstruction layer is broken [21]. When we deal the active layer with Plasma (Ar/H₂O) treatment, the Fe atoms in core parts and adjacent-surface would be simultaneously excited migrating into active layer, further optimizing the surface structure. Taking the advantages of these two paths Fe migration, abundant effective Ni-O-Fe units may be obtained to improve the electron transfer ability between metal active sites.

3.1. Structural characterization of F-FN-NFO

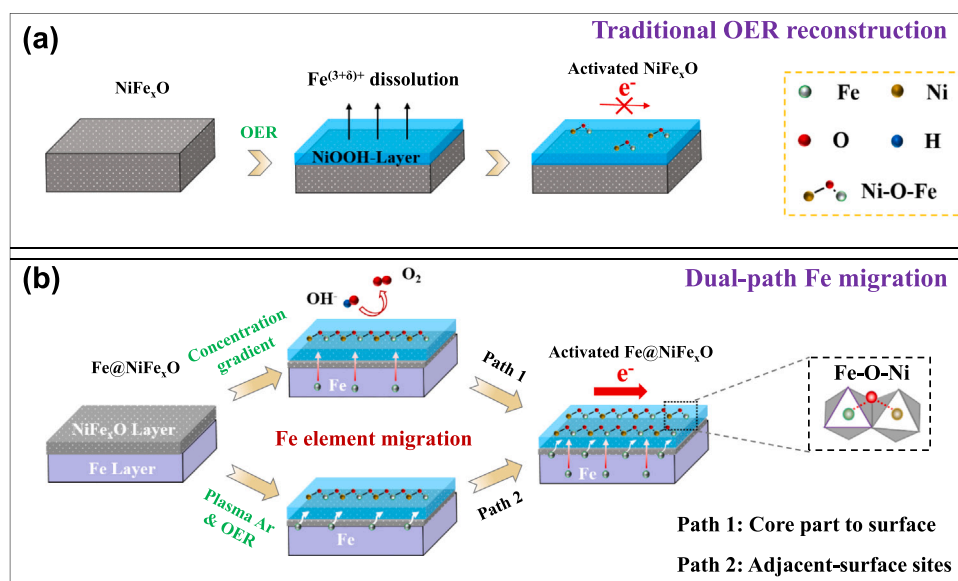
The preparation of F-FN-NFO model electrode is displayed in Experiment Section and its characterization is revealed in Fig. 1. X-ray diffraction (XRD) result shows the characteristic peaks at $2\theta = 44.2^\circ$, 51.5° and 75.8° in patterns of FeNi₃ can be indexed to (111), (200) and (220) lattice planes (PDF #38-0419), respectively (Fig. 1a). The undiscovered FN-NFO signal is attribute to the micro-content or low-crystallinity, which can be proved by High-resolution transmission electron microscopy (HR-TEM) and Element mapping

results. Scanning electron microscopy (SEM) images demonstrate that the synthesized electrode has a clear layered structure with smooth surface on the Ti substrate in Fig. 1b. HR-TEM image in Fig. 1c shows that a core-shell structure on surface with the ordered lattice fringes, which has been partial enlarged in Fig. 1d. As shown in Fig. 1d (i), clear lattice fringes with an interplanar spacing of 0.254 and 0.210 nm are index to the (311) and (400) plane of Fe₃O₄, respectively. Similarly, the distinct lattice fringes with an interplanar spacing of 0.246 and 0.208 nm can be indexed to the (111) and (200) plane of NiO in Fig. 1d (ii), respectively. What's more, the spacing of 0.206 nm of inner layer corresponds to the (111) plane of FeNi₃ in Fig. 1d(iii). Fig. 1e displays the element mapping results, it is obviously seen that a layered structure with evenly distributed Ni/Fe/O signals in surface and only Fe and O signals in inner parts, indicates the adjacent surface of synthesized sample is of FeNi₃@NiO-Fe₃O₄ core-shell structure with a dramatic Fe concentration gradient.

To further confirm the composition and structure of the sample, we performed X-ray photoelectron spectroscopy (XPS) tests with in situ etching. As shown in Fig. 2a, the synthesized sample can be divided into three layers (L-I, L-II, L-III), in which the main components in L-I are NiO and Fe₃O₄ (Fig. 4a, b) while obvious Ni and Fe signals appeared in L-II (etching for 90 s). It is noteworthy that the Fe/Ni ratios in both L-I and L-II are low. With continuous etching for 240 s, the Ni content sharply decreased and it turns into nearly pure Fe phase in L-III layer. Combining XRD, XPS and HR-TEM results, the surface species of the produced sample contains NiO and Fe₃O₄ in surface, FeNi₃ in adjacent surface and metal Fe in bulk, which presents obvious Fe concentration gradient distribution. Thus, the synthesized F-FN-NFO model electrode is named as Fe@FeNi₃@NiO-Fe₃O₄.

3.2. Dual-path Fe migration promotes the stepwise reconstruction of Ni-O-Fe units

The effect of dynamic deposition of Fe from the electrolyte on the components of NiFe based catalysts have been first investigated, the point of OER activity and XPS results in Fig. S2 strongly support the idea that the dynamic dissolution and redeposition of Fe in our work can hardly increase the Fe content on the surface of FN-NFO-p electrodes. Thus, we further study the rule of elements migration in OER process based on the synthesized F-FN-NFO catalysts, and FN-NFO electrode was



Scheme 1. Schematic of the stepwise reconstruction of Ni-O-Fe units on the reactivated F-FN-NFO catalyst. (a) Traditional OER reconstruction process, most of the electron transfer units between heterogeneous metals are destruct. (b) ‘Dual-path Fe migration’ strategy for the reconstruction of Ni-O-Fe electron transfer channels in active layer.

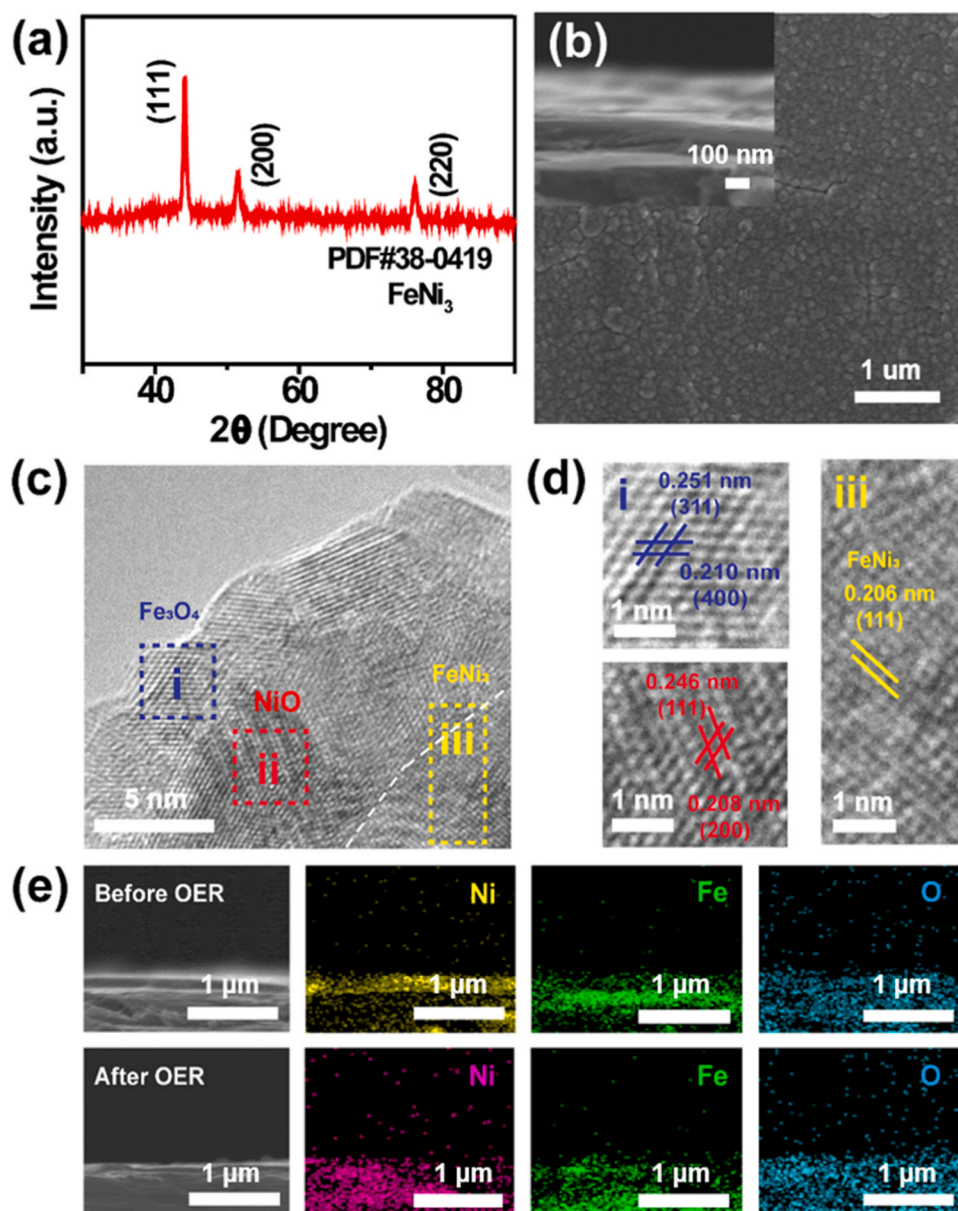


Fig. 1. Characterization of F-FN-NFO. (a) XRD. (b) SEM image of the surface, the inset corresponding to the cross-section. (c, d) TEM images, i, ii and iii correspond to the HR-TEM images of Fe_3O_4 , NiO and FeNi_3 , respectively. (e) Element mapping patterns of the cross-section before and after OER. (f-i) In situ XPS etching on the surface of sample with etching speed of 40 nm min^{-1} : (f) F-FN-NFO before OER, (g) FN-NFO after OER, (h) FN-NFO-p (Plasma $\text{Ar}/\text{H}_2\text{O}$ treatment on the OER reconstructed FN-NFO) after OER and (i) F-FN-NFO after OER. The OER refers to 100 CV cycles at 0–0.8 V vs. Ag/AgCl .

prepared for comparison. The XPS in situ etching results for the samples before and after OER are shown in Fig. 2b–d and S1. Compared Figs. 2b and 2c, the Fe/Ni ratio increased significantly at the etching depth of 10 nm when the reconstructed FN-NFO electrode was treated with plasma $\text{Ar}/\text{H}_2\text{O}$ technology and OER activated (named as FN-NFO-p), but it remained unchanged at the deeper etching position. The statistical rule of intensity ration of $\text{Fe}/(\text{Ni}+\text{Fe})$, $\text{O}/(\text{Ni}+\text{Fe}+\text{O})$ in FN-NFO and FN-NFO-p before and after OER (Fig. S3a, b, e, f) confirms that the plasma treatment would not only promote the partly oxidation of samples (Fig. 2f and S3a), but also induce the redistribution of Fe element near the surface (Fig. S3e, f). This phenomenon indicates that Fe atom migration occurs at the adjacent-surface sites in the FN-NFO-p electrode. Beside, Fig. S4a–d, S4g shows that the ration of $\text{Fe}/\text{Fe-O}$ in FN-NFO-p increased near surface and slowly decreased in deeper sites after OER compared to that before OER, proves that more metal Fe atoms rather than Fe ions migrated to surface from the inner part during OER when the sample is treated with plasma, which is caused by oxygen atoms occupying part of the Fe sites in the inner parts. Different from FN-NFO and FN-NFO-p, the Fe/Ni concentration distribution in F-FN-NFO has an obvious change in L-II layer after OER, and the Fe/Ni ration increases

significantly when the etch deep reaches 60 nm (Fig. 2d). In contrary, the Fe/Ni ratio nearly unchanged in L-II layer of FN-NFO before and after OER. Fig. S4c, g indicates that Fe content increases in the whole oxidation parts with a concentration gradient change, corresponding to the directional Fe migration from bulk to surface. It is noted that the ration of $\text{Fe}/\text{Fe-O}$ in various depth of F-FN-NFO nearly unchanged in this process (Fig. S4e and black line in Fig. S4h), meaning that the dynamic migrated Fe can be easier oxidation to drive its directional migration. In summary, the F-FN-NFO and FN-NFO-p electrode demonstrate various Fe element migration paths during OER, more metal Fe atoms migrated near the surface in path 1 (plasma treatment), and more Fe-O species directional migrate in path 2 (directional migration from bulk to surface).

Combining the characteristics of the above two methods, a stepwise plasma $\text{Ar}/\text{H}_2\text{O}$ treatment was performed on the F-FN-NFO electrode during CV cycling (labelled as F-FN-NFO-p, 0–0.8 V vs. Ag/AgCl at 10 mV s^{-1}). The change of Ni/Fe atomic ratio on the surface was analyzed by XPS technology in Fig. S5. It can be seen that the initial Ni/Fe ratio of F-FN-NFO increases from 3.08 to 3.31 after 100 CV cycles, which derives from the loss of Fe on the surface. When treated it with

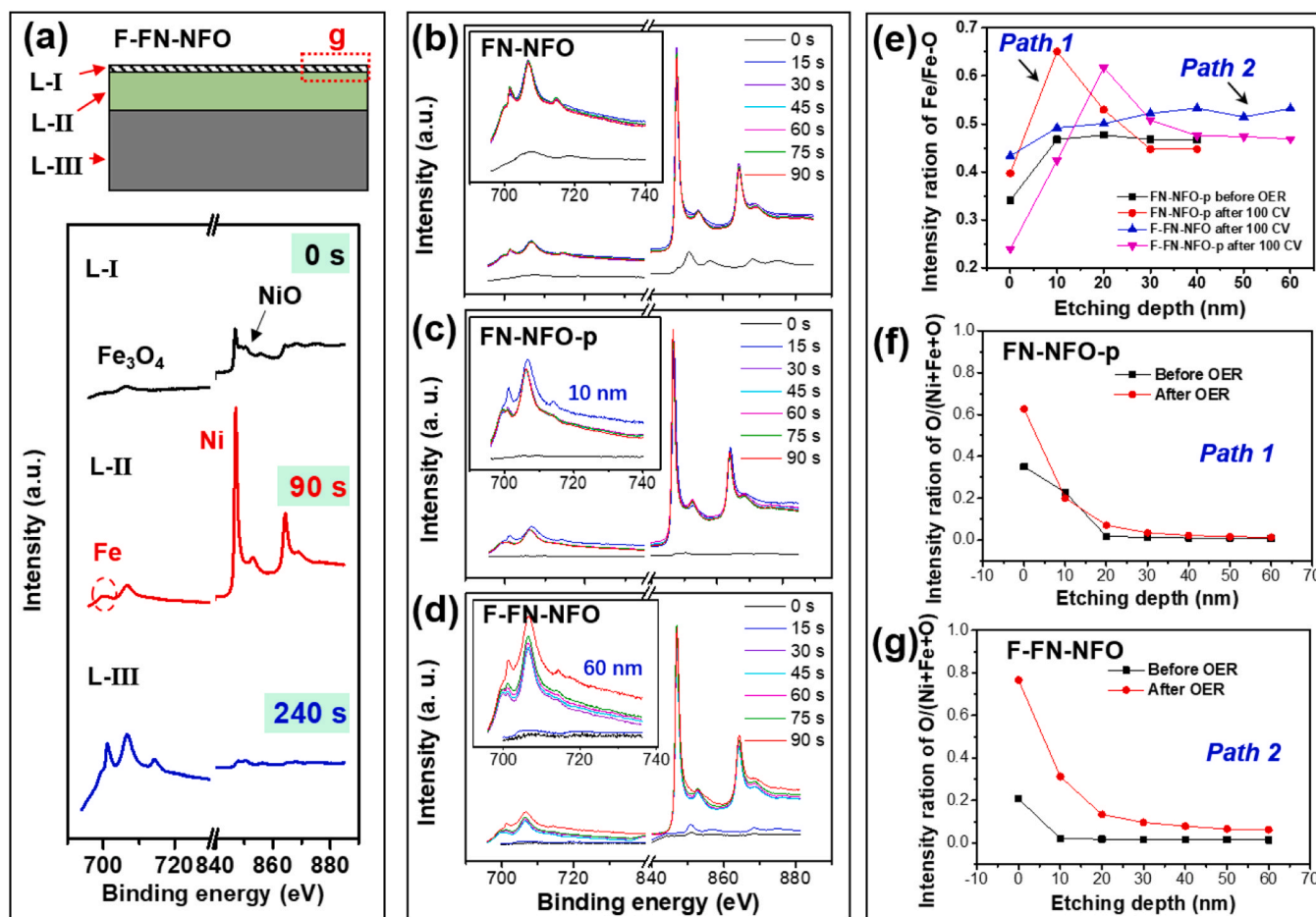


Fig. 2. In situ XPS etching on the surface of sample with etching speed of 40 nm min^{-1} : (a) F-FN-NFO before OER, (b) FN-NFO after OER, (c) FN-NFO-p (Plasma Ar/ H_2O treatment on the OER reconstructed FN-NFO) after OER and (d) F-FN-NFO after OER. The OER refers to 100 CV cycles at 0–0.8 V vs. Ag/AgCl. (e) Comparison of ratio of Fe/Fe-O in various etching depth of FN-NFO-p, F-FN-NFO and F-FN-NFO-p before and after OER. The distribution of O element in various etching depth of (f) FN-NFO-p and (g) F-FN-NFO before and after OER.

plasma Ar/ H_2O technique, the Ni/Fe ratio of F-FN-NFO-p₁ surface fast reduces to 2.10, which ascribes to the expose of metal sites in adjacent-surface layer. However, the experiment result is far lower than the theoretical value of phase separation (Ni/Fe=2.85), which confirms the direction Fe migration to surface of F-FN-NFO in OER. The subsequent reaction follows a similar rule but slacken the decrease of Ni/Fe value, which means that the element distribution tends to become stable in the next surface reconstruction. Further more, the F-FN-NFO-p sample in Fig. S3g, h and S4f, h show typical characters of both FN-NFO-p and F-FN-NFO. The difference is that the oxidation rate of migrated metal Fe in path 1 is strengthened by the effect of direction migration in path 2 (Fig. 2e).

Then, we compared the OER performance of FN-NFO, FN-NFO-p and F-FN-NFO-p electrodes with CV cycling (Fig. 3a-c and S6). Fig. 3a shows obvious instability of original FN-NFO electrode after 300 CV cycles. When treated the FN-NFO electrode with plasma Ar/ H_2O technique after 100 CV cycles intervals, Fig. 3b demonstrates a certain improvement of OER activity for FN-NFO-p electrode. But it suffers from a soon active downtrend with a further activation. Then, a similar treatment is carried out on F-FN-NFO electrode, as shown in Fig. 3c. The activity of F-FN-NFO-p electrode significantly improves after two times plasma Ar/ H_2O treatments, which is much higher than FN-NFO and FN-NFO-p electrodes. The activity change rules of the above three electrodes are summarized in Fig. 3h. The activity of both FN-NFO and FN-NFO-p fluctuates with periodic plasma Ar/ H_2O treatment, while F-FN-NFO-p electrode shows a stepwise increase with Fe element migration. After the

300 CV scanning cycles, the oxygen evolution activity of F-FN-NFO-p increases 8.6 times, from 30.5 mA cm^{-2} to 263 mA cm^{-2} at 1.7 V vs. RHE.

To explore the essential reasons for the different change of OER performance in three electrodes, we tracked the surface active units of samples with various treatments by time-track Raman spectroscopy. As presented in Fig. 3d-g, two Raman characteristic signals of Ni-O at 490 and 554 cm^{-1} are indexed to the E_g bending vibration ($\delta(\text{Ni-O})$) and A_1g stretching vibration ($\nu(\text{Ni-O})$) modes in NiOOH lattice structure, respectively [17]. Generally, NiOOH contains β and γ phases with different intensity ratio of $\nu(\text{Ni-O})/\delta(\text{Ni-O})$ (abbreviated as $I_{\delta/\nu}$), the higher $I_{\delta/\nu}$ corresponding to γ -NiOOH with much disorder structure, and the lower $I_{\delta/\nu}$ indicates β -NiOOH species with high OER activity. Besides, the vibration peak around 681 cm^{-1} index to $\nu(\text{Ni-O-Fe})$ [17]. For traditional FN-NFO electrode (Fig. 3d), the $I_{\delta/\nu}$ rapid decreases after the initial 100 CV cycling, it indicates completely transformation from γ -NiOOH into high activity β -NiOOH. But the $\nu(\text{Ni-O-Fe})$ suffers from an obvious reduction, limiting the improvement of OER performance. For FN-NFO-p sample, Fig. 3e displays a similar decrease of $I_{\delta/\nu}$ corresponding to the generation of abundant β -NiOOH species in OER process. Besides, the peak intensity of $\nu(\text{Ni-O-Fe})$ decreases after plasma Ar/ H_2O treatment, but it is largely strengthened with a distinct characteristic peak at 752 cm^{-1} generated at the followed OER activation. It is notice that the newly formed peak significantly shifts to higher wave numbers compared to typical FeOOH stretching vibrations reported in the literature [17]. D. L. A. de Faria claimed that it can be ascribed to the

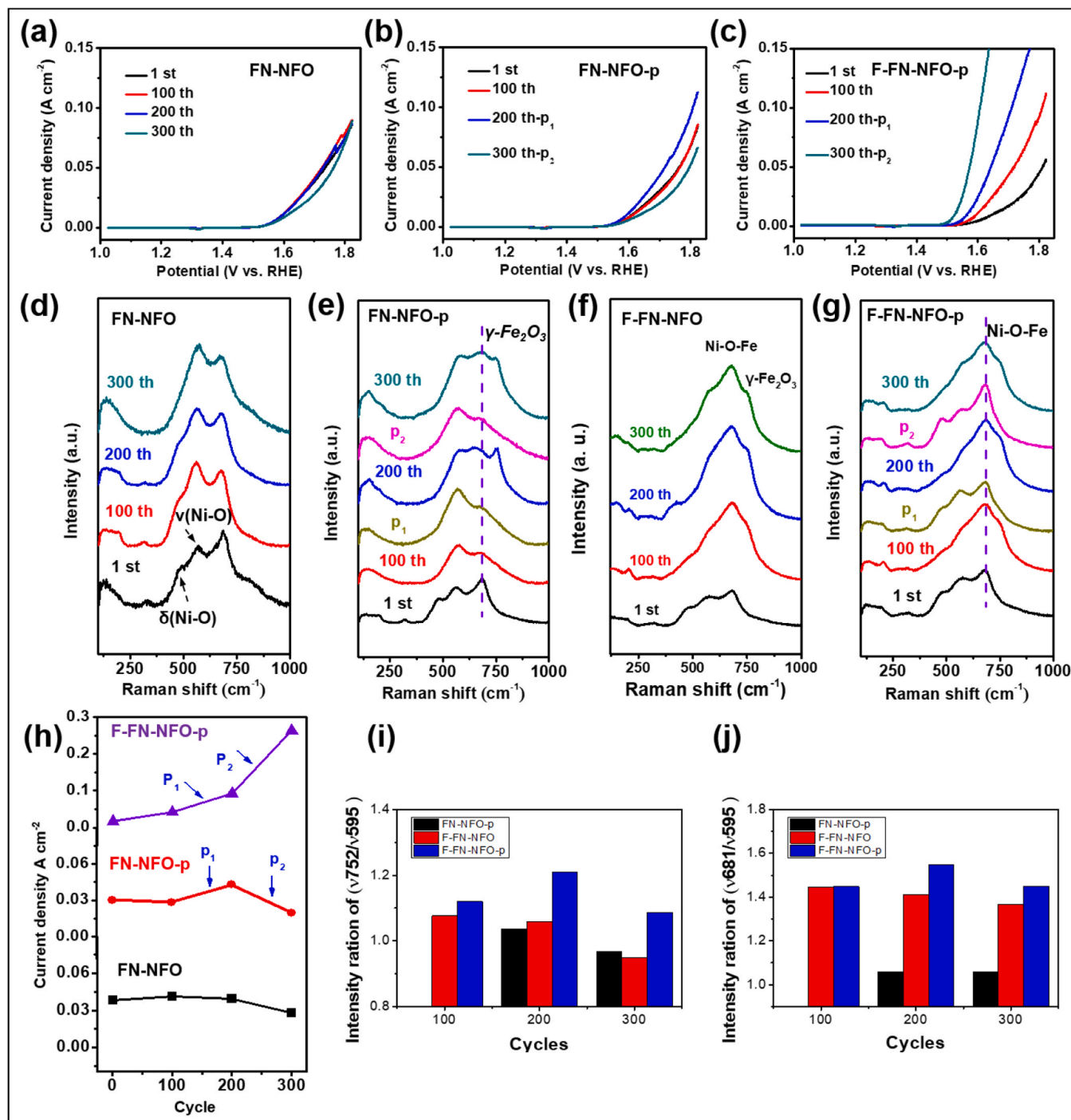


Fig. 3. OER evaluation process and the corresponding time-track Raman spectra of FN-NFO, FN-NFO-p and F-FN-NFO-p electrodes. (a-c) CV test in pH=14 KOH electrolyte at a scan rate of 10 mV s⁻¹ of three electrodes: (a) FN-NFO, (b) FN-NFO-p and (c) F-FN-NFO, in which p₁ and p₂ represent the first and second plasma Ar/H₂O treatments, respectively. (d-g) Time-track Raman spectra: (d) FN-NFO, (e) FN-NFO-p and (f) F-FN-NFO (g) F-FN-NFO-p under the periodic surface treatment with CV cycling and plasma Ar/H₂O. (h) The activity of the three electrodes changes at 1.6 V. The intensity ratio of (i) ν752/ν595 (γ-Fe₂O₃) and (j) ν681/ν595 (Ni-O-Fe) in various samples after every 100 CV cycles.

partly generation of γ-Fe₂O₃ (maghemite) in surface, which has inverse spinel structure with 2.67 Fe defects in octahedral sites of each unit cell (Fe_{21.33}□_{2.67}O₃₂) [22]. Based on above discussion, the adjacent-surface Fe migration would promote the formation of γ-Fe₂O₃ in active layer for constructing more Ni-O-Fe units. For F-FN-NFO as shown in Fig. 3f, the vibration signals of γ-Fe₂O₃ appear in all the OER process, which is due to the directional Fe migration from core to surface. But it disappeared when treated with plasma Ar/H₂O treatment shown in Fig. 3g, the

changes of ν(γ-Fe₂O₃) and ν(Ni-O-Fe) are similar with FN-NFO-p electrode (take A_{1g} as a reference). After the stepwise activation, the peak intensity of ν(Ni-O-Fe) is significantly enhanced, which is consistent with the improvement of OER performance. The intensity ratio of ν752/ν595 (γ-Fe₂O₃) and ν681/ν595 (Ni-O-Fe) Fig. 3i and 3j are significantly enhanced by combining plasma treatment and CV cycling, it means that the directional Fe migration can promote the formation of Ni-O-Fe units, which would be largely strengthened by further

combining the adjacent-surface migration of Fe atoms.

To further explore the activation mechanism of Fe migration in path 1 and path 2, Operando Raman test between 0.1 and 0.7 V vs. RHE was performed for the samples before and after 100 CV cycles (Fig. S7 a-h). Fig. S7i and S7j shows the 555/475 peak intensity ratio at 0.7 V vs. Ag/AgCl of the synthesized samples and the corresponding formation voltage of NiOOH, respectively. The $\nu_{555/475}$ nearly the same for the initial FN-NFO-p, F-FN-NFO and F-FN-NFO-p samples before CV test, but it demonstrates much different after 100 CV cycles with the order as FN-NFO < FN-NFO-p < F-FN-NFO < F-FN-NFO-p. It is noted that the intensity ration of $\nu_{555/475}$ in F-FN-NFO-p is much higher than the other samples, means abundant β -NiOOH generated on the surface of F-FN-NFO-p during OER. Besides, F-FN-NFO-p also shows the lowest formation voltage of NiOOH. In conclusion, the dual-path Fe migration plays a vital role for constructing Ni-O-Fe units, which bridges the β -NiOOH and γ -Fe₂O₃ clusters for dramatically enhancing the OER activity of catalyst.

The changes of electron structure on different reaction stages of F-FN-NFO-p are further investigated by XPS technology (Fig. 4). Ni 2p XPS spectra is shown in Fig. 4a, two dominant spin-orbit peaks in original F-FN-NFO corresponding to Ni²⁺ specie (located at 855.5 and 873.5 eV) and Ni specie (located at 852.0 and 869.4 eV), respectively. After the first 100 CV cycles, a pair of new peaks are distinguished at 856.1 and 873.7 eV that indicates Ni³⁺ species in NiOOH. Then, the Ni³⁺/Ni²⁺

ratio dramatically increases at the followed plasma Ar/H₂O treatment (first time, p₁), which prefer to occupy the octahedral interstices sites in Ni-O-Fe units [23]. With the further CV cycling, the content of Ni²⁺ reversely enhanced and then kept stable in p₁-200th-p₂-300th process, indicating a high reversibility of Ni ions in the valence state changes after surface treatment. Similarly, Fig. 4b shows a partly reversible transformation between Fe₃O₄ and Fe³⁺ in Fe 2p XPS spectrum. In CV cycling, the kind of Fe species proceed (Fe₃O₄ → Fe³⁺), while the reverse transition (Fe³⁺ → Fe₃O₄) appeared after plasma Ar/H₂O treatment. HR-TEM results in Fig. S8 also corroborates that the disappeared Fe₃O₄ crystallinity in CV cycling is regenerated after plasma Ar/H₂O treating. It illustrates that the surface treatment by plasma Ar/H₂O can promote the Fe atomic rearrangement in active layer with altering the valence state of metal ions. In addition, Fig. 4c shows the O 1s XPS spectra, the deconvolution shows three characteristic peaks at 529.8, 531.2, and 532.2 eV (marked as O-I, O-II, and O-III), assigning to the lattice oxygen, oxygen vacancies and adsorbed H₂O, respectively. After 100th CV cycles, the O-I area is significantly decline that responds to the lattice oxygen activation in OER. However, both I_{O-I}/I_{O-II} and I_{O-I}/I_{O-III} appreciably increases after plasma Ar/H₂O treatment, indicating the adsorbed H₂O dissociates and binds with the uncoordinated metal cations. Then, the content of O-I remains stable in the follow treating process, declaring the dynamic equilibrium of lattice oxygen release and recombination in

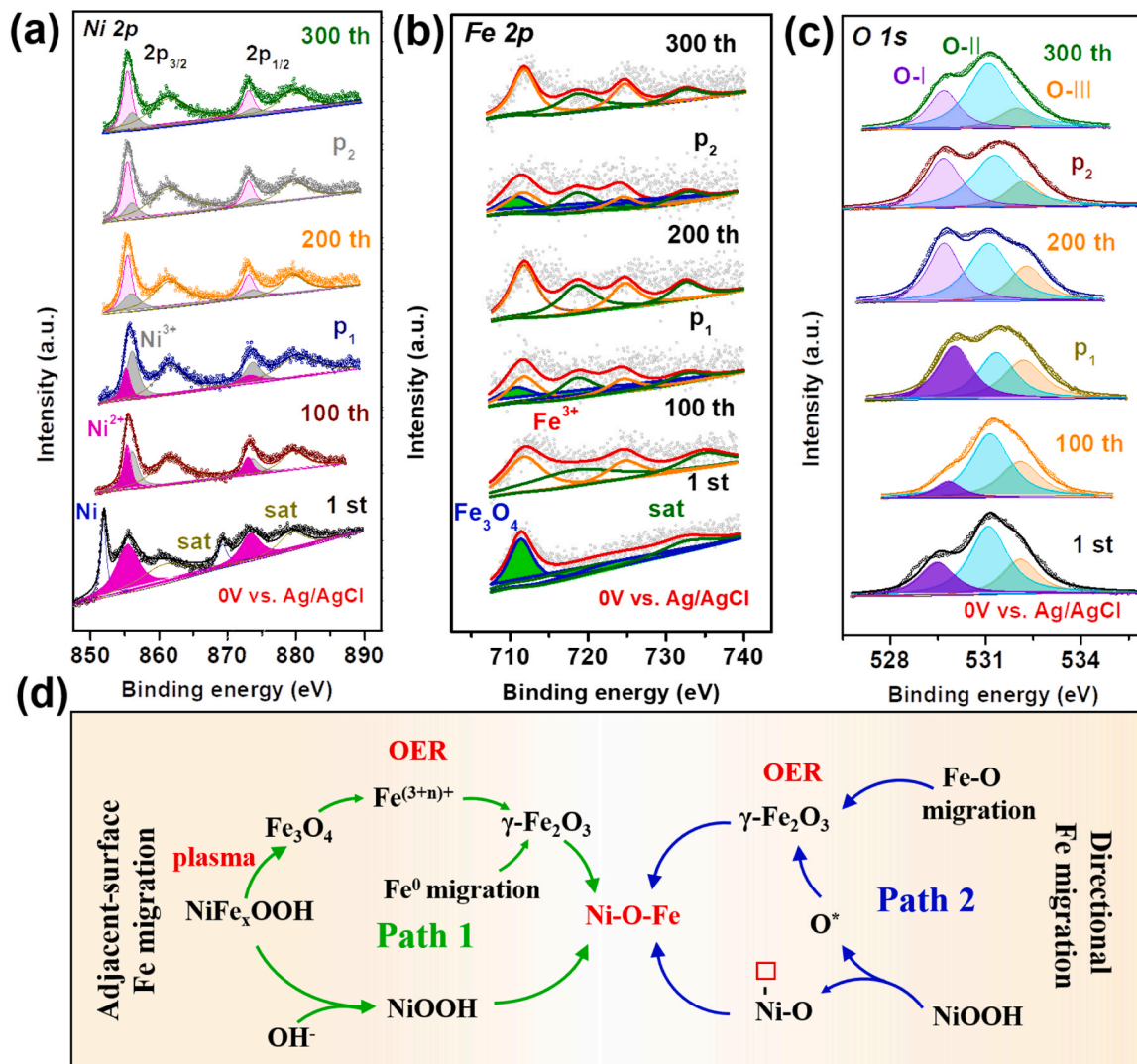


Fig. 4. The XPS spectra of F-FN-NFO electrode with intermittent plasma Ar/H₂O and OER activation treatments (a) Ni 2p and (b) Fe 2p and (c) O 1s XPS spectra. (d) Scheme of the two paths Fe element migration for constructing Ni-O-Fe units in the surface of F-FN-NFO.

OER. Combining the analysis of XPS with Raman results, two migration paths of Fe element in surface reconstruction of F-FN-NFO can be summarized, as shown in Fig. 4d. In adjacent-surface Fe migration after Plasma Ar/H₂O treated (Path 1), Fe₃O₄ is separated from NiFe_xOOH, and it further transformed into Fe⁽³⁺ⁿ⁾⁺ reacting with the migrated Fe⁰, the generated γ -Fe₂O₃ further forms a heterojunction with NiOOH to construct Ni-O-Fe units. In directional Fe migration (Path 2), the migrated Fe-O species from core part is firstly oxidized by the activated lattice oxygen, forming γ -Fe₂O₃ that further composes with the activated

NiOOH to build Ni-O-Fe units. Due to the dual-path Fe migration in OER, abundant Ni-O-Fe units are stepwise reconstructed in the active surface.

3.3. DFT calculation and analysis of Ni-O-Fe repair mechanism

Based on the dual-path Fe migration process, abundant Ni-O-Fe units are constructed in surface active layer. In order to reveal the formation mechanism, γ -Fe₂O₃/β-NiOOH and γ -FeOOH/β-NiOOH heterojunctions are selected as models to calculate the interface formation

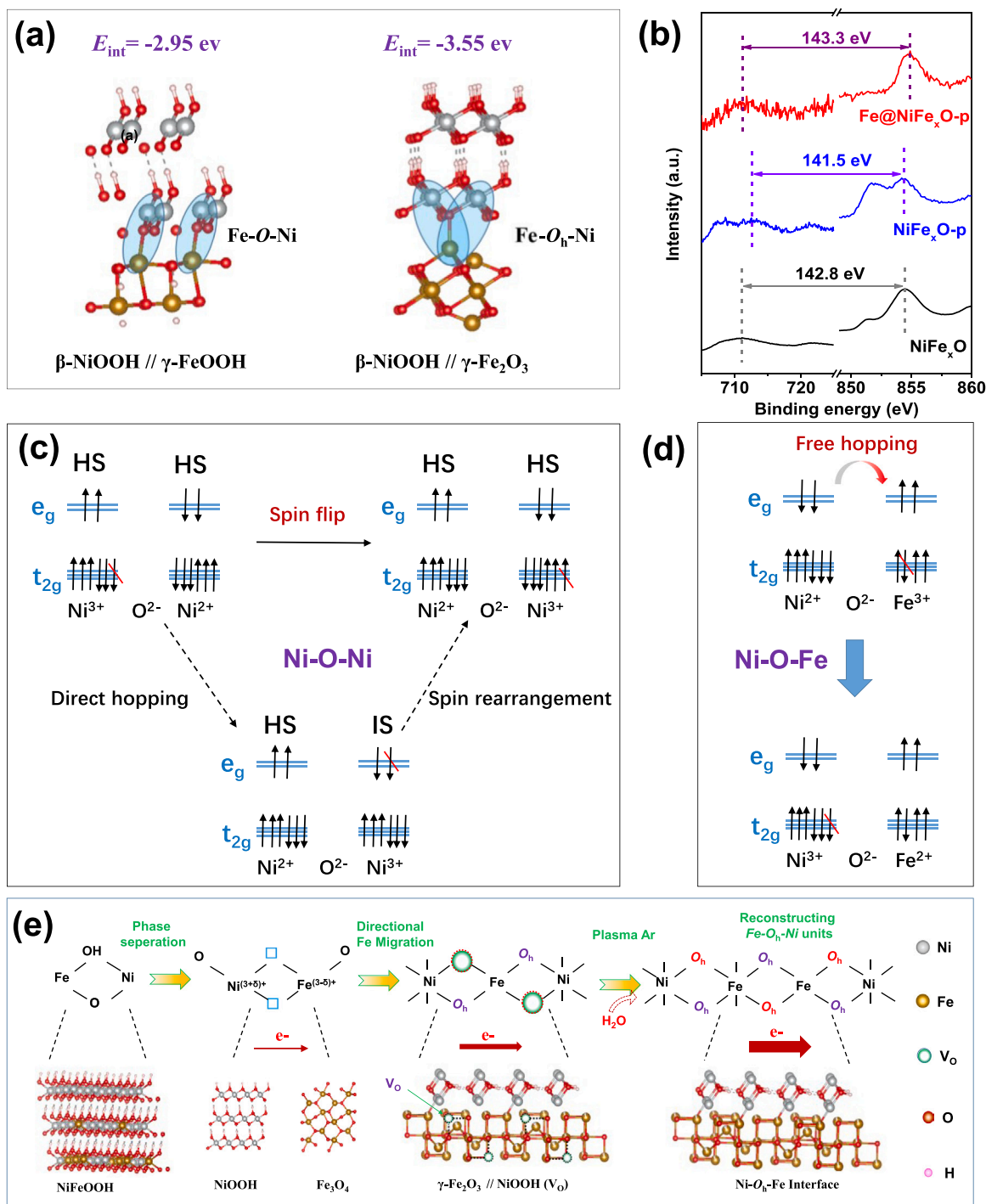


Fig. 5. (a) DFT calculation on the interfacial energy of β -NiOOH // γ -Fe₂O₃ and NiOOH // γ -FeOOH heterostructure. (b) Surface XPS spectra of the three electrodes after 300 CV cycles, which presents a better electron transfer ability of F-FN-NFO-p electrode after activated. (c) Carrier/hole hopping with spin-flip between adjacent Ni²⁺/Ni³⁺ in Ni-O-Ni. (d) Free hopping between Ni²⁺/Fe³⁺ in Ni-O-Fe units. (e) The repair process of PET channels in F-FN-NFO-p during OER reconstruction.

energy by Density Functional Theory (DFT), respectively. As shown in Fig. 5a, the interface formation energy of $\gamma\text{-Fe}_2\text{O}_3/\beta\text{-NiOOH}$ (-3.55 eV) is much lower than $\gamma\text{-FeOOH}/\beta\text{-NiOOH}$ (-2.95 eV), it means the surface $\beta\text{-NiOOH}$ is prefer to combine with $\gamma\text{-Fe}_2\text{O}_3$ for forming Ni-O-Fe units. Thus, the dual-path Fe migration can promote the construction of Ni-O-Fe units. In addition, the optimized model of $\gamma\text{-Fe}_2\text{O}_3/\beta\text{-NiOOH}$ demonstrates typical octahedral structure oxygen ($\mu\text{-O}_h$) to bridge the Ni-O-Fe structure. Theoretically, partial electron transfer (PET) can be triggered in different metal center with bridged $\mu\text{-O}_h$ through π -donation, which is believed to be one of the key factors for electron redistribution [14]. Fig. 5b shows that F-FN-NFO-p electrode has a higher red shift of Ni 2p peak and blue shift of Fe 2p peak compared to the other two electrodes, indicating better electron transfer ability of F-FN-NFO-p electrode after activated. The carrier transportation process is shown in Figs. 5c and 5d, when select $\mu\text{-O}_h$ symmetry of hexa-coordinated MO_6 as a model, the valence electron configurations of Ni^{2+} , Ni^{3+} , Fe^{2+} and Fe^{3+} can be typically identified to be $3d^8 (t_{2g}^6 e_g^2)$, $3d^7 (t_{2g}^5 e_g^2)$, $3d^6 (t_{2g}^4 e_g^2)$, $3d^5$ (high-spin (HS), $t_{2g}^3 e_g^2$), respectively. For traditional FN-NFO electrode, a dense NiOOH layer on the surface of catalysts is believed as the active sites, in which a hole needs to be transferred between two adjacent Ni ions (Fig. 5c). By flipping the spin of the hole, the process can also be considered as two

virtual steps: one is the hole transfers from the left Ni to the right one keeping the spin to make an intermediate spin state (IS) Ni^{3+} ; the other one is the IS Ni^{3+} turn to be HS one with a spin rearrangement [15]. Therefore, extra energy is needed for the carrier transportation by the spin-flip hopping process. For the activated F-FN-NFO-p electrode with Ni-O-Fe as active units, the less occupation of d orbital in Fe^{3+} would increase the carrier mobility by avoiding spin-flip hopping process [17]. The repair process of PET channels in F-FN-NFO-p during OER reconstruction is distinguished in Fig. 5e. The carrier migration ability of PET channels can be considered as $\text{Fe}^{2+}\text{-O-Ni}^{3+} < \text{Fe}^{3+}\text{-O-Ni}^{2+}$ (Fig. S9). For the initial F-FN-NFO, there are only NiO and Fe_3O_4 species with lower content of $\mu\text{-O}_h$ forming $\text{Fe}^{2+}\text{-O-Ni}^{3+}$ channels, the corresponding PET is the weakest. After directional Fe migration in OER (path 2), the generated $\text{Fe}^{3+}\text{-O-Ni}^{3+}$ units is separated by the abundant $\mu\text{-O}_h$ defects (by-products), limiting the further improvement of PET between the heterojunction. With the further Plasma Ar/ H_2O treatment (path 1), the lacked $\mu\text{-O}_h$ is replenished to significantly strengthen the PET in the followed CV cycling (>200 cycles). For a long time working, the improved PET can accelerate the compensation efficiency of lattice oxygen in OER process to keep the structure stable. Herein, the ability of electron transfer in Ni-O-Fe units is well optimized by dual-path Fe migration to improve OER performance.

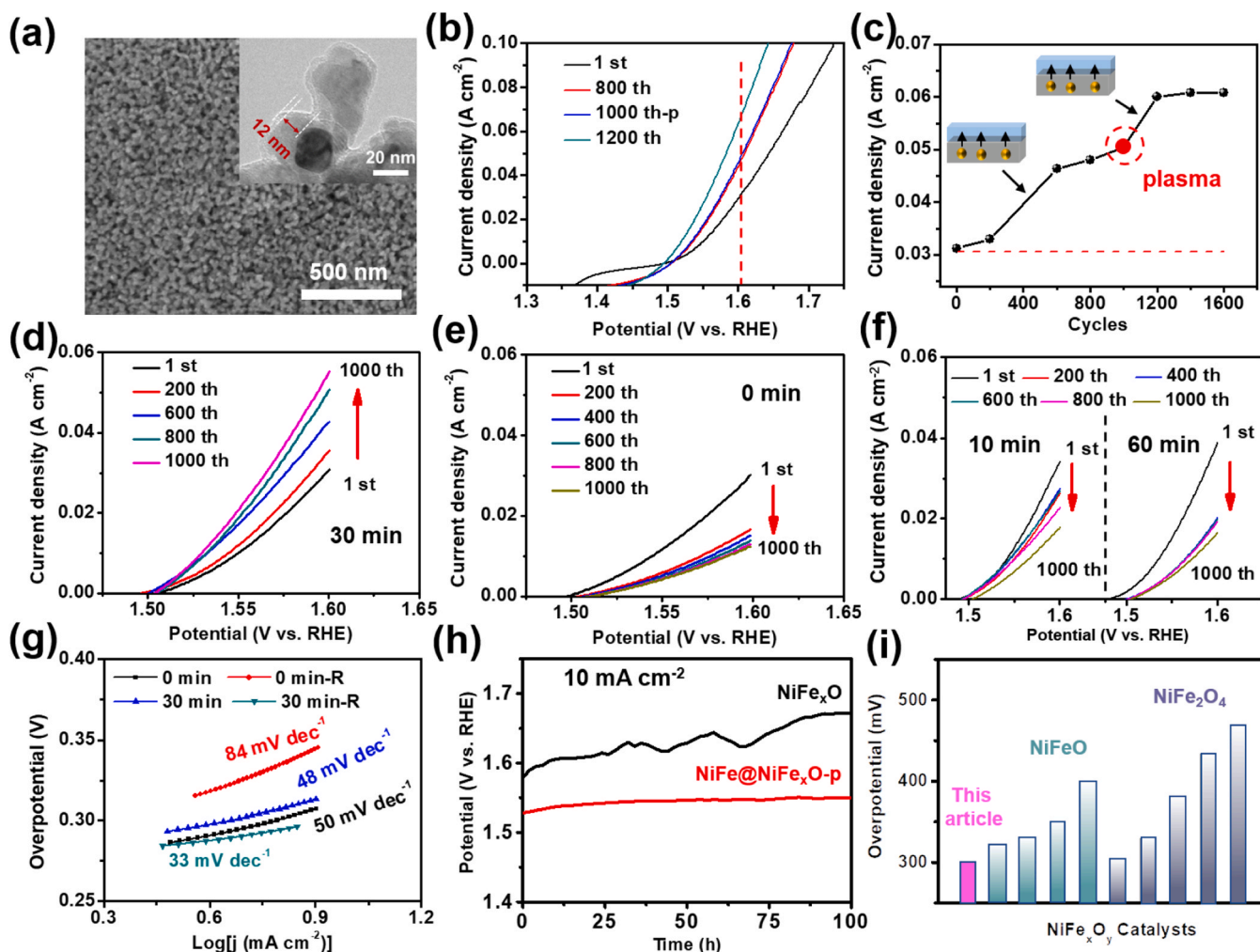


Fig. 6. Characterization and electrochemical evaluations of the synthesized three-dimensional $\text{NiFe@NiFe}_x\text{O}$ electrodes. (a) Structure and morphology of $\text{NiFe@NiFe}_x\text{O}$ annealed for 30 min, the insert is TEM image. (b) OER performance evaluation of $\text{NiFe@NiFe}_x\text{O}$ – 30 min after CV cycles and plasma Ar/ H_2O treatment. (c) The corresponding stepwise changes of the OER activity tested at 1.6 V. (d–f) The CV activation process of $\text{NiFe@NiFe}_x\text{O}$ with various annealing time: (d) 30 min, (e) 0 min, (f) 10 and 60 min (g) The corresponding Tafel slope for $\text{NiFe@NiFe}_x\text{O}$ – 0 min and $\text{NiFe@NiFe}_x\text{O}$ – 30 min before and after OER, in which ‘0 min’, ‘30 min’ and ‘-R’ in the represent ‘no annealing’, ‘30 min annealing’ and ‘after OER’, respectively. (h) Chronopotentiometry curves of FN-NFO and $\text{NiFe@NiFe}_x\text{O}$ -p at 10 mA cm^{-2} . (i) The comparison of the prepared electrode to the other NiFe oxides [24–32].

3.4. Application of the 'dual element migration' strategy on three-dimensional NiFe@NiFe_xO and inert NiV@NiV_xO electrodes

Then, a series of self-supporting three-dimensional NiFe@NiFe_xO electrodes with Fe concentration gradient were prepared by the annealing and chemical etching technology. The synthesized electrodes is only 0.04 mm (1/30 of Ni foam, Fig. S10) with a higher electrical conductivity (714 S/m, higher than carbon paper, nickel foam and stainless steel net) and higher yield strength (up to 1 Mpa). As shown in Fig. 6a and S11, abundant cross-linked pores with an average size around 5–10 nm distribute in the designed NiFe@NiFe_xO sample. Adjusting the annealed time to 30 min, the insert image in Fig. 6a demonstrates an obvious three-layer core-shell structure in the sample, including a 3 nm thick surface layer and a 12 nm thick middle layer. XPS in situ etching results confirm the gradient distribution of Fe element from core to shell (Fig. S12). XRD and EDS results prove that the synthesized electrodes is composed of FeNi₃, NiO and Fe₃O₄ with the evenly distribution of Ni, Fe, and O elements on surface (Fig. S13). By adjusting the heat treatment time (0 min, 10 min, 30 min and 60 min), TEM results show that the middle layer is positive expanded until it completely diffused to the surface (Fig. S14a-c).

The activity and stability of NiFe@NiFe_xO electrodes are further evaluated by repeat CV cycling and chronoamperometry tests. As shown in Fig. 6b, the OER performance of NiFe@NiFe_xO electrode reached stable after 1000 CV cycles at the first step activation. After treating the electrode with plasma Ar/H₂O (named as 1000-p), the OER performance further increases at the subsequent 200 CV cycles (marked as 1200th in picture). After the stepwise activation process, the OER overpotential would be reduced to 299 mV at current density of 10 mA cm⁻², and the activity can be improved from 31 to 63 mA cm⁻² at 1.6 V vs. RHE (Fig. 6c, S19a). Then we adjusted the concentration gradient of NiFe@NiFe_xO to optimize oxygen evolution efficiency by controlling the annealing time (Fig. S18). With increases the annealing time, the OER activity experiences a change of slow decline-increase-fast decline at 1.6 V vs. RHE (Fig. 6d-f and S14d). Specifically, the OER activity of electrode annealed for 30 min (named as NiFe@NiFe_xO -30 min) shows a significant increase during CV cycles (1 st-1000 th in Fig. 6d), while the unannealed FN-NFO experienced a sharply decrease (Fig. 6e). In the meantime, the change of tafel slope is consistent with above results, the NiFe@NiFe_xO -30 min electrode shows the best reaction kinetics (Fig. 6g). In order to reveal the main reason for the change in activity, we performed XPS characterization on the surface and the inside of both FN-NFO and NiFe@NiFe_xO -30 min before and after CV cycling. After 1000 CV cycles, the proportion of Ni²⁺/Ni³⁺ on the surface of NiFe@NiFe_xO -30 min nearly unchanges while the interior obviously decreases, indicating that the corresponding electron transfer ability on the surface is enhanced after Fe element migration (Fig. S15). What's more, the content ratio of surface lattice oxygen vs. oxygen defects remained relatively stable before and after OER, proving the high stability of active layer in OER evolution (Fig. S16). As a compared electrode, FN-NFO presents a decrease ratio of Ni²⁺/Ni³⁺ corresponding to the weakened electron transfer ability (Fig. S17). To evaluate the electrochemical stability of the stepwise activated NiFe@NiFe_xO -30 min electrode (abbreviated as NiFe@NiFe_xO -p), Fig. 6h displays the chronopotentiometry test with an ultrahigh stability for more than 100 h at the current density of 10 mA cm⁻². After 100 h reaction, the micro-composition and structure of sample also be characterized by XPS, SEM and TEM. Fig. S19 shows that the sample still keeps porous structure though it comes much rough. Besides, the metal sites on surface have been oxidized to high valence for both Ni (Ni³⁺) and Fe (Fe³⁺), and more lattice oxygen formed compared to the initial sample. Such a structure guarantee the stability of surface structure in NiFe@NiFe_xO during OER. Furthermore, we compared the obtained electrode to the other NiFe based oxides previous reported, Fig. 6i and Table S1 demonstrate that the as prepared NiFe@NiFe_xO -p electrode exhibits a much more competitiveness OER activity and stability.

At the same time, we monitor the oxygen evolution reaction of inert NiV@NiV_xO according to the above method (Fig. S20b, S21). After 200 CV cycles, the performance of NiV@NiV_xO slightly increases and reaches to the first platform. Obviously, this state does not represent the best oxygen evolution performance of NiV@NiV_xO. Therefore, an analogous stepwise activation process has been done, the overpotential of NiV@NiV_xO electrode further reduced from 383 to 320 mV at the current density of 10 mA cm⁻² with a small tafel slope of 44 mV dec⁻¹. This results prove that the strategy has a potential application in modifying the inert electrode.

4. Conclusion

In conclusion, a dual-path Fe element migration in Fe@NiFeO_x is well controlled by step-wise surface treatment in OER process, which significantly promotes the reconstruction of Ni-O-Fe channels for electron density redistribution. The directional Fe migration can help form the γ-Fe₂O₃/NiOOH heterostructure in the surface activated layer to reduce the formation energy of Ni-O-Fe units, while the adjacent-surface Fe migration would further optimize the electron transfer channel and stabilize such a structure. After surface reconstruction, the OER activity increases 8.6 times at 1.7 V (30.5–263 mA cm⁻²) compared to the pre-designed sample. Based on this strategy, the activity of three-dimension NiFe@NiFe_xO electrodes have been improved by twice with stable working for more than 100 h at 10 mA cm⁻² current density.

CRedit authorship contribution statement

Xiaobing Wang: Conceptualization, Data curation, Formal analysis, Investigation, Methodology, Writing- original draft, Funding acquisition. **Chengyu Wei:** Data curation, Investigation, Methodology. **Xiaosheng Song:** Software. **Zuohui Wang:** Supervision, Validation, Review. **Yong Zhao:** Funding acquisition.

Declaration of Competing Interest

The authors declare that they have no known competing financial interests or personal relationships that could have appeared to influence the work reported in this paper.

Data availability

No data was used for the research described in the article.

Acknowledgements

Xiaobing Wang and Chengyu Wei contributed equally to this work. This work is financially supported by National Natural Science Foundation of China (21773055), and Key Research & Development and Promotion Project of Henan Province (Science and Technology Tackling Key Problems, 192102310468).

Appendix A. Supporting information

Supplementary data associated with this article can be found in the online version at doi:10.1016/j.apcatb.2023.123279.

References

- [1] Y. Liu, L.J. Wang, H. Zhang, H.Y. Yuan, Q. Zhang, L. Gu, H.F. Wang, P. Hu, P.F. Liu, Z. Jiang, H.G. Yang, Boosting photocatalytic water oxidation over bifunctional Rh⁰-Rh³⁺ sites, *Angew. Chem. Int. Ed.* 60 (2021) 22761–22768.
- [2] J. Zhang, J. Cui, S. Eslava, Oxygen evolution catalysts at transition metal oxide photoanodes: their differing roles for solar water splitting, *Adv. Energy Mater.* 11 (2021) 2003111.
- [3] D. Zhao, Z. Zhuang, X. Cao, C. Zhang, Q. Peng, C. Chen, Y. Li, Atomic site electrocatalysts for water splitting, oxygen reduction and selective oxidation, *Chem. Soc. Rev.* 49 (2020) 2215–2264.

- [4] S. Chen, M. Zhang, P. Zou, B. Sun, S. Tao, Historical development and novel concepts on electrolytes for aqueous rechargeable batteries, *Energy Environ. Sci.* 15 (2022) 1805–1839.
- [5] M.F. Lagadec, A. Grimaud, Water electrolyzers with closed and open electrochemical systems, *Nat. Mater.* 19 (2020) 1140–1150.
- [6] S.H. Ye, Z.X. Shi, J.X. Feng, Y.X. Tong, G.R. Li, Activating CoOOH porous nanosheet arrays by partial iron substitution for efficient oxygen evolution reaction, *Angew. Chem. Int. Ed.* 57 (2018) 2672–2676.
- [7] Z.-P. Wu, X.F. Lu, S.-Q. Zang, X.W. Lou, Non-noble-metal-based electrocatalysts toward the oxygen evolution reaction, *Adv. Funct. Mater.* 30 (2020) 1910274.
- [8] L. Gao, X. Cui, C.D. Sewell, J. Li, Z. Lin, Recent advances in activating surface reconstruction for the high-efficiency oxygen evolution reaction, *Chem. Soc. Rev.* 50 (2021) 8428–8469.
- [9] H. Jiang, Q. He, Y. Zhang, L. Song, Structural self-reconstruction of catalysts in electrocatalysis, *Acc. Chem. Res.* 51 (2018) 2968–2977.
- [10] B.R. Wygant, K. Kawashima, C.B. Mullins, Catalyst or precatalyst? the effect of oxidation on transition metal carbide, pnictide, and chalcogenide oxygen evolution catalysts, *ACS Energy Lett.* 3 (2018) 2956–2966.
- [11] S. Jin, Are metal chalcogenides, nitrides, and phosphides oxygen evolution catalysts or bifunctional catalysts? *ACS Energy Lett.* 2 (2017) 1937–1938.
- [12] J. Liu, L. Guo, In situ self-reconstruction inducing amorphous species: a key to electrocatalysis, *Matter* 4 (2021) 2850–2873.
- [13] F. Dionigi, P. Strasser, NiFe-based (oxy)hydroxide catalysts for oxygen evolution reaction in non-acidic electrolytes, *Adv. Energy Mater.* 6 (2016) 1600621.
- [14] J. Jiang, F. Sun, S. Zhou, W. Hu, H. Zhang, J. Dong, Z. Jiang, J. Zhao, J. Li, W. Yan, M. Wang, Atomic-level insight into super-efficient electrocatalytic oxygen evolution on iron and vanadium co-doped nickel (oxy)hydroxide, *Nat. Commun.* 9 (2018) 2885.
- [15] Z. Li, J. Yang, Z. Chen, C. Zheng, L.Q. Wei, Y. Yan, H. Hu, M. Wu, Z. Hu, V “bridged” Co□O to eliminate charge transfer barriers and drive lattice oxygen oxidation during water-splitting, *Adv. Funct. Mater.* 31 (2021) 2008822.
- [16] J.Y.C. Chen, L. Dang, H. Liang, W. Bi, J.B. Gerken, S. Jin, E.E. Alp, S.S. Stahl, Operando analysis of nife and fe oxyhydroxide electrocatalysts for water oxidation: detection of Fe^{4+} by mössbauer spectroscopy, *J. Am. Chem. Soc.* 137 (2015) 15090–15093.
- [17] J. Chen, F. Zheng, S.-J. Zhang, A. Fisher, Y. Zhou, Z. Wang, Y. Li, B.-B. Xu, J.-T. Li, S.-G. Sun, Interfacial interaction between FeOOH and Ni-Fe LDH to modulate the local electronic structure for enhanced oer electrocatalysis, *ACS Catal.* 8 (2018) 11342–11351.
- [18] W. Yan, Y. Shen, C. An, L. Li, R. Si, C. An, FeOx clusters decorated hcp Ni nanosheets as inverse electrocatalyst to stimulate excellent oxygen evolution performance, *Appl. Catal. B-Environ.* 284 (2021), 119687.
- [19] X. Liu, J. Meng, J. Zhu, M. Huang, B. Wen, R. Guo, L. Mai, Comprehensive understandings into complete reconstruction of precatalysts: synthesis, applications, and characterizations, *Adv. Mater.* 33 (2021) 2007344.
- [20] C. Wei, N. Heng, Z. Wang, X. Song, Z. Sun, X. Zhu, J. He, Y. Zhao, X. Wang, Dynamic active site evolution and stabilization of core-shell structure electrode for oxygen evolution reaction, *Chem. Eng. J.* 435 (2022), 134672.
- [21] X. Liu, J. Meng, K. Ni, R. Guo, F. Xia, J. Xie, X. Li, B. Wen, P. Wu, M. Li, J. Wu, X. Wu, L. Mai, D. Zhao, Complete reconstruction of hydrate pre-catalysts for ultrafast water electrolysis in industrial-concentration alkali media, *Cell Rep. Phys. Sci.* 1 (2020), 100241.
- [22] D.L.A. de Faria, S. Venâncio Silva, M.T. de Oliveira, Raman microspectroscopy of some iron oxides and oxyhydroxides, *J. Raman Spectrosc.* 28 (1997) 873–878.
- [23] X. Yue, X. Qin, Y. Chen, Y. Peng, C. Liang, M. Feng, X. Qiu, M. Shao, S. Huang, Constructing active sites from atomic-scale geometrical engineering in spinel oxide solid solutions for efficient and robust oxygen evolution reaction electrocatalysts, *Adv. Sci.* 8 (2021) 2101653.
- [24] A. Mahmood, Q. Yu, Y. Luo, Z. Zhang, C. Zhang, L. Qiu, B. Liu, Controllable structure reconstruction of nickel-iron compounds toward highly efficient oxygen evolution, *Nanoscale* 12 (2020) 10751–10759.
- [25] J. Qiao, F. Song, J. Hu, D. Huo, J. Yuan, J. Shen, L. Niu, A.-j Wang, Mesoporous spinel NiFe oxide cubes as advanced electrocatalysts for oxygen evolution, *Int. J. Hydrogen Energ.* 44 (2019) 16368–16377.
- [26] Y. Cheng, S. Dou, J.-P. Veder, S. Wang, M. Saunders, S.P. Jiang, Efficient and durable bifunctional oxygen catalysts based on nifeo@mnox core-shell structures for rechargeable Zn-air batteries, *ACS Appl. Mater. Interfaces* 9 (2017) 8121–8133.
- [27] R. Wei, X. Bu, W. Gao, R.A.B. Villaos, G. Macam, Z.-Q. Huang, C. Lan, F.-C. Chuang, Y. Qu, J.C. Ho, Engineering surface structure of spinel oxides via high-valent vanadium doping for remarkably enhanced electrocatalytic oxygen evolution reaction, *ACS Appl. Mater. Interfaces* 11 (2019) 33012–33021.
- [28] P. Ramakrishnan, K. Beom Lee, G.-J. Choi, I.-K. Park, J. Inn, Sohn, Porous hollow nanorod structured chromium-substituted inverse spinel compound: an efficient oxygen evolution reaction catalyst, *J. Ind. Eng. Chem.* 101 (2021) 178–185.
- [29] V.D. Silva, L.S. Ferreira, T.A. Simões, E.S. Medeiros, D.A. Macedo, 1D hollow MFe_2O_4 ($\text{M} = \text{Cu}, \text{Co}, \text{Ni}$) fibers by Solution Blow Spinning for oxygen evolution reaction, *J. Colloid Interface Sci.* 540 (2019) 59–65.
- [30] L. Cao, Z. Li, K. Su, M. Zhang, B. Cheng, Rational design of hollow oxygen deficiency-enriched NiFe_2O_4 @N/rGO as bifunctional electrocatalysts for overall water splitting, *J. Energy Chem.* 54 (2021) 595–603.
- [31] W. Zong, D. Rao, H. Guo, Y. Ouyang, Y.-E. Miao, W. Wang, J. Wang, F. Lai, T. Liu, Gradient phosphorus-doping engineering and superficial amorphous reconstruction in NiFe_2O_4 nanoarrays to enhance the oxygen evolution electrocatalysis, *Nanoscale* 12 (2020) 10977–10986.
- [32] J. Zhao, X. Zhang, M. Liu, Y.-Z. Jiang, M. Wang, Z.-Y. Li, Z. Zhou, Metal-organic-framework-derived porous 3D heterogeneous $\text{NiFe}_x/\text{NiFe}_2\text{O}_4$ @NC nanoflowers as highly stable and efficient electrocatalysts for the oxygen-evolution reaction, *J. Mater. Chem. A* 7 (2019) 21338–21348.